Dalton Transactions

Accepted Manuscript

ROYAL SOCIETY OF CHEMISTRY

www.rsc.org/dalton

Cite this: DOI: 10.1039/c0xx00000x

www.rsc.org/xxxxxx

ARTICLE TYPE

Hollow mesoporous $NiCo_2O_4$ nanocage as efficient electrocatalysts for oxygen evolution reaction†

Xiaoming Lv, Yihua Zhu,* Hongliang Jiang, Xiaoling Yang,* Yanyan Liu, Yunhe Su, Jianfei Huang, Yifan Yao and Chunzhong Li

Received (in XXX, XXX) Xth XXXXXXXXX 20XX, Accepted Xth XXXXXXXXX 20XX
DOI: 10.1039/b000000x

The design and fabrication of efficient and inexpensive electrodes for oxygen evolution reaction (OER) is essential for energy-conversion technologies. Herein, high OER activity is achieved using hollow mesoporous $NiCo_2O_4$ nanocages synthesized via a Cu_2O-templated strategy combined with coordination reaction. The $NiCo_2O_4$ nanostructures with hollow cavity, large roughness and high porosity show only a small overpotential of ~0.34 V at the current density of 10 mA cm^{-2} and a Tafel slope of 75 mV $decade^{-1}$, which is comparable with the performance of the best reported transition metal oxide based OER catalysts in previous literatures. Meanwhile, the positive impacts of the nanocage structure and the Ni incorporation on the electrocatalytic performance are also demonstrated by comparing the OER activities of $NiCo_2O_4$ nanocages with Co_3O_4 nanocages, $NiCo_2O_4$ nanoparticles and 20 wt% Pt/C. Moreover, the $NiCo_2O_4$ nanocages also manifest superior stability to other materials. All these merits indicate that the hollow mesoporous $NiCo_2O_4$ nanocages are promising electrocatalyst for water oxidation.

1. Introduction

With the increasing demand for clean and sustainable energy, great efforts have been devoted to alternative energy conversion and storage systems with high efficiency, low cost and environmental safety. Electrochemical water splitting provides an attractive path to produce hydrogen (H_2) fuels and store electricity.[1-4] However, large-scale electrochemical water splitting is greatly hindered by the sluggish anodic oxygen evolution reaction (OER) which usually has slow kinetics and requires large overpotentials.[5-7] Therefore, an appropriate oxygen evolution catalyst is essential to accelerate the reaction rate and lower the overpotential. To date, IrO_2 and RuO_2 have been the most active OER catalysts, operating in acidic and alkaline solutions.[8-10] However, their applications are limited owing to the high cost and scarcity of the precious metals.[11-13] Therefore, extensive research effort has been devoted to developing highly active, durable and low-cost OER catalysts.

Recently, spinels and transition metal oxides are becoming more and more popular. Co_3O_4 and its substituted cobaltites have been demonstrated to be promising electroactive materials because of their good catalytic activity and corrosion stability for electrochemical OER in alkaline media.[14-20] To improve the electrochemical activity of Co_3O_4 electrocatalysts, researchers have incorporated Ni atoms into the spinel structure to form $NiCo_2O_4$, which enhances electrical conductivity of the metal oxide and increased the number of catalytically active sites.[21-23] Till now, $NiCo_2O_4$, a mixed valence oxide that adopts a spinel structure, has gained much research interest as an efficient oxygen evolution catalyst.

The structures of electrode materials strongly affect their performance. Previous studies have shown that Co-based spinel oxides for OER are usually in the form of thin films or particle agglomerates bound together by polymers.[19-20, 24-25] For such structures, electrocatalytic activity is significantly limited by the small surface area and poor electron-mass transfer. To address this situation, some structures for OER process have been reported such as nanowire array,[14] hierarchical nanorod,[26] mesoporous nanoplatelet/graphene[27] and so on. However, synthesizing effective OER catalyst with large surface area and efficient electron-mass transfer still remains a challenge.

Lately, hollow structures have attracted great attention because of the intrinsic advantages of building blocks and additional benefits resulting from the secondary architecture.[28-30] Specifically, anisotropic nanocages with non-spherical shapes and regular interiors are of particular interest for their designable morphology, low density, large void space, high surface area and shell permeability, which gives them potential use for application in catalysis.[31-33] However, to our best knowledge, it is quite rare on the reports of synthesizing hollow $NiCo_2O_4$ nanocages, let alone the application for OER catalysis.

Herein, we have synthesized hollow $NiCo_2O_4$ octahedral nanocages via the Cu_2O-templated strategy combined with coordination reaction. The electrochemical activities of $NiCo_2O_4$ nanocages towards OER were also investigated. The $NiCo_2O_4$ nanostructures exhibited high OER electrocatalytic activity with low overpotential, high current density and high stability owing to its unique morphology and composition.

2. Experimental section

2.1. Reagents and materials

Poly(vinyl pyrrolidone) (PVP, Mw = 40000) was purchased from Sigma-Aldrich. Copper chloride dihydrate ($CuCl_2·2H_2O$), sodium citrate ($C_6H_5O_7Na_3.2H_2O$), glucose ($C_6H_{12}O_6$) sodium hydroxide (NaOH), nitric acid (HNO_3), cobalt chloride hexahydrate ($CoCl_2.6H_2O$), nickel chloride hexahydrate ($NiCl_2·6H_2O$) were all obtained from Shanghai Lingfeng Chemical Reagent Co. All the chemicals were used as received. All aqueous solutions were prepared using deionized (DI) water with a resistivity of 18 MΩ·cm.

2.2. Preparation of solid Cu_2O crystals

Cu_2O templates were synthesized by a modified method as described in Lou's work.[34] In a typical procedure, 10 ml of an aqueous solution of NaOH (2 M) was added dropwise into 100 mL of a mixture solution containing $CuCl_2·2H_2O$ (10 mM), sodium citrate (3.4 mM) and PVP (Mw = 40000, 0.04 g mL^{-1}) under stirring. After 0.5 h, 10 ml of ascorbic acid solution (0.6 M) was added dropwise into the above solution. The suspension was further aged at 33 °C for 2.5 h to produce Cu_2O octahedral with edge length of 250 nm. The resulting products were harvested by several rinse-centrifugation cycles with DI water and ethanol for further characterization.

2.3. Preparation of amorphous $(NiCo_x)O(OH)$ octahedral

In a typical procedure, Cu_2O templates (10.0 mg), $NiCl_2·6H_2O$ (0.57 mg), $CoCl_2·6H_2O$ (1.13 mg) were added into the ethanol/water mixed solvent (10.0 mL, volume ratio = 1:1) in the presence of PVP (Mw = 40000, 0.34g). After the mixture was stirred for 10 min, 4 mL $Na_2S_2O_3$ aqueous solution (1 M) was added dropwise. Then the reaction was carried out at room temperature for 10 min until the suspension solution changed from red to green-yellow. Eventually, the resulting product $(NiCo_x)O(OH)$ was harvested by several rinse-centrifugation cycles with deionized water and ethanol, and finally dried at room temperature for further characterization.

2.4. Preparation of hollow $NiCo_2O_4$ nanocages

In a typical procedure, the produced $(NiCo_x)O(OH)$ material was successively annealed in air atmosphere at 400 °C for 2 h with a slow ramp rate of 1 °C min^{-1} to make the hollow $NiCo_2O_4$ nanocages.

2.5. Preparation of Co_3O_4 nanocages

For the synthesis of Co_3O_4 nanocages, most of the procedure is the same as the procedure for preparing the $NiCo_2O_4$ nanocages except that the 0.57 mg $CoCl_2·6H_2O$ and 1.13 mg $NiCl_2·6H_2O$ were replaced by 1.7 mg $CoCl_2·6H_2O$. The precipitates were separated by centrifugation, washed with DI water and ethanol, and dried under vacuum overnight.

2.6. Preparation of $NiCo_2O_4$ nanoparticles

$NiCo_2O_4$ nanoparticles were synthesized by a method similar to that for the preparation of $NiCo_2O_4$ nanocages but without the addition of PVP. The precipitates were separated by centrifugation, washed with DI water and ethanol, and dried under vacuum overnight.

2.7. Measurements and characterizations

The morphology and microstructure of all samples were examined by transmission electron microscopy (TEM: JEM-2100, operated at 200 kV) equipped with an energy dispersive X-ray analyzer (EDX) and scanning electron microscopy (FE-SEM: S-4800). X-ray power diffraction (RIGAK, D/MAX 2550 VB/PC, Japan) was used to investigate crystalline structure. Brunauer-Emmett-Teller (BET) models were used to determine the specific surface areas, pore volume, and the pore sizes of the samples. X-ray photoelectron spectroscopy (XPS) was conducted using VG ESCA 2000 with an Mg Kα as source and the C 1s peak at 284.6 eV as an internal standard.

2.8. Catalytic performance measurement

The procedures of pretreatment for glass carbon rotating disk electrode (3 mm in diameter) and modification are as follows: prior to use, the working electrode is polished mechanically with 0.5 μm down to 0.05 μm alumina slurry to obtain a mirror-like surface and then washed with Mill-Q water and acetone and allowed to dry. 5 mg of catalyst powder was dispersed in 1 mL of 3:1 （v/v） water/2-propanol mixed solvent with 40 μL of Nalfion solution (5 wt%, Sigma-Aldrich), and then the mixture was ultrasonicated for about 1 h to generate a homogeneous ink. Next, 10 μL of the dispersion was transferred onto the glassy carbon rotating disk electrode (RDE) (5 mm in diameter, Pine Research Instrumentation), leading to the catalyst loading ~0.25 mg cm^{-2}. Finally, the as-prepared catalyst film was dried at room temperature for electrochemical measurement.

Electrochemical experiments were conducted using CHI660C advanced electrochemical system. A conventional three-electrode cell was employed incorporating a working glass carbon, an Ag/AgCl, KCl (3.5 M) electrode as reference electrode, and a Pt electrode as counter electrode. All potentials were measured and reported vs. the Ag/AgCl, KCl (3.5 M) reference electrode. The electrode is allowed to dry at room temperature before measurement. 0.1 M KOH aqueous solution saturated with oxygen by bubbling O_2 for 30 min served as the supporting electrolyte. All the potentials versus the Ag/AgCl (3.5 M KCl) reference electrode were converted to the reversible hydrogen electrode (RHE) scale via the Nernet equation:[35]

$$E_{RHE} = E_{Ag/AgCl} + 0.059\ pH + E^{\theta}_{Ag/AgCl} \quad (1)$$

Where E_{RHE} is the converted potential versus RHE, $E_{Ag/AgCl}$ is the experimental potential measured against the Ag/AgCl reference electrode, and $E^{\theta}_{Ag/AgCl}$ is the standard potential of Ag/AgCl (3.5 M KCl) at 25 °C (0.205 V). The electrochemical measurements were carried out in 0.1 M KOH (pH =13) at room temperature: therefore, $E_{RHE} = E_{Ag/AgCl} + 0.973$ V.

The cyclic voltammetry (CV) curves were conducted by sweeping the potential from -0.9 to 1 V vs. Ag/AgCl at room temperature and 1600 rpm. All the data were recorded after applying a number of potential sweeps until which were stable. The polarization curves were obtained by sweeping the potential from 0 to 0.9 V (vs. Ag/AgCl) with a sweep rate of 10 mV s^{-1} at 1600 rpm. The OER potential was IR corrected using E - iR relation, where i is the current and R is the uncompensated electrolyte ohmic resistance, which was measured via high-frequency AC impedance. The accelerated stability tests for OER were performed in O_2-saturated 0.1 M KOH at room temperature by potential cycling between 0.3 V and 0.9 V (vs. Ag/AgCl) at a sweep rate of 100 mV s^{-1} for 500 cycles. At the end of the cycles, the resulting electrodes were used for polarization curves at a

sweep rate of 10 mV s^{-1}.

3. Results and discussion

The synthesis strategy of hollow mesoporous $NiCo_2O_4$ nanocage is illustrated in Scheme 1. In the first step, highly uniform Cu_2O octahedral crystals were synthesized by reducing a copper-citrate complex solution with ascorbic acid in the presence of polyvinylpyrrolidone (PVP). Afterwards, $(NiCo_x)O(OH)$ shell structure started to form and Cu_2O was etched according to a "coordinating etching and precipitating" (CEP) process.[36] Finally, thermal treatment facilitates to produce hollow $NiCo_2O_4$ nanocage.

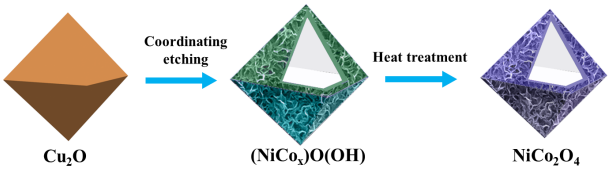

Scheme 1. Schematic diagram of the fabrication of hollow mesoporous $NiCo_2O_4$ nanocages.

Fig. 1 presents typical SEM and TEM images of the obtained Cu_2O templates and $(NiCo_x)O(OH)$ precursor. The Cu_2O shows a uniform octahedral structure with an length of ca. 250 nm, as shown in Fig. 1a, 1b. Fig. 1c, 1d reveal that the cage-like $(NiCo_x)O(OH)$ has an octahedral structure which inherits the geometrics and dimensions of the Cu_2O templates. It can be clearly observed from Fig. 1d that the structures of $(NiCo_x)O(OH)$ are wormlike, as small particles constituting the shell structure are active and easily aggregate to form varying degrees of secondary structures on the surface of the cage to reduce the system energy. The interior and architectural construction of the as-prepared $(NiCo_x)O(OH)$ nanocages have been further studied by TEM, as displayed in Figure 1e, 1f, The inner cavity is clearly revealed by the contrast between the shells and hollow interiors. The shell of the nanocages is as thin as ~15 nm. Because of the equally high reactivity of the eight faces of the Cu_2O octahedron,[36, 37] no structural deformation such as warping or collapse occurs though the reaction proceeds quite quickly.

After simple thermal treatment of the as-synthesized $(NiCo_x)O(OH)$ nanocages, $NiCo_2O_4$ nanocages were readily obtained. The crystal structure of the obtained product was examined by means of X-ray diffraction (XRD). Figure S1 presents the XRD pattern of the as-synthesized $NiCo_2O_4$ nanocages. The diffraction peaks agree well with the standard patterns of the spinel $NiCo_2O_4$ phase (JCPDF card no. 20-0781).[38,39] The overview SEM images and low-magnification TEM images (Figure 2) show that the as-prepared $NiCo_2O_4$ nanostructures consist of uniform nanocages without small particles even after calcination. Figure 2b reveals that the cage-like $NiCo_2O_4$ still maintains octahedral geometries and dimensions of the relevant $(NiCo_x)O(OH)$ nanocages except for a little shrinkage in size, which is ca. 200 nm. The octahedral shell structures can be observed obviously from the SEM image in Figure 2b. Moreover, the broken particles in the inset of Figure 2a show their hollow structure. The low-magnification TEM image in Figure 2c shows the hollow nanocages with visible hollow interior structure. Especially, a typical nanocage with well-defined interior and very thin shell can also be detected, which is in good agreement with the SEM analysis. The thickness of shell is ca. 20 nm. The SAED pattern (Figure 2c inset) shows the polycrystalline features of the $NiCo_2O_4$ nanocages. Additionally, the HRTEM image (Figure 2d) also detects the lattice spacing (0.248 nm), which agrees with the (311) plane spacing of $NiCo_2O_4$ with a spinel structure, in agreement with the XRD results.

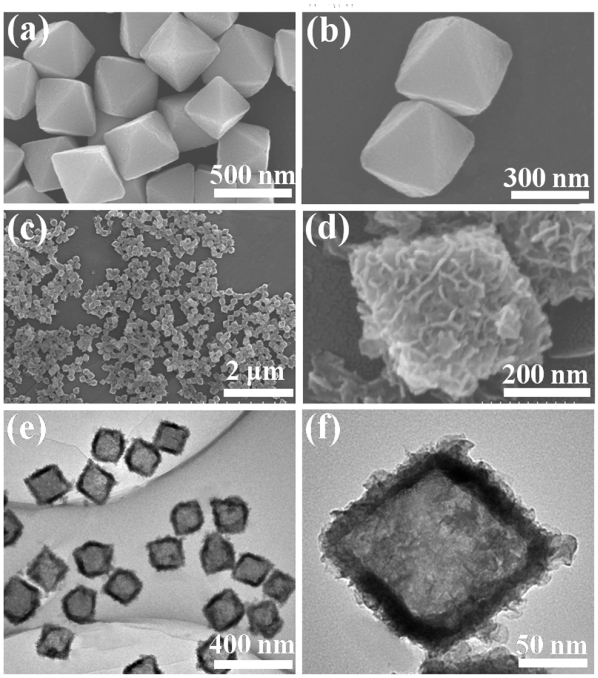

Figure 1. SEM images of (a, b) Cu_2O octahedral with an average edge length of 250 nm and (c, d) octahedral $(NiCo_x)O(OH)$ precursors by simultaneous coordinating etching of Cu_2O templates; (e, f) TEM images of $(NiCo_x)O(OH)$ structures.

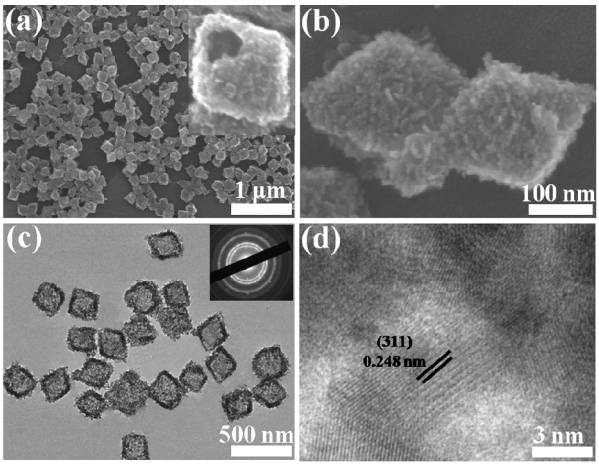

Figure 2. SEM images (a, b), TEM images (c) and HRTEM images (d) of as-synthesized hollow $NiCo_2O_4$ nanocages yielded by calcinations at 400 ℃. The inset in (c) is the selected area electron diffraction (SAED).

In addition, we also applied energy dispersive X-ray spectroscopy (EDX) and element mapping analysis to characterize the composition of the $NiCo_2O_4$ nanocages. The elemental composition of the octahedron nanocages measured by EDX is shown in Figure 3a, which suggests that the product

contains Ni, Co and O elements with the atomic ratio of Ni to Co being approximately 1:2. This is consistent with the element mapping analysis. Figure 3b-f show the representative STEM images of hollow $NiCo_2O_4$ octahedrons and the corresponding Ni, Co and O elemental mapping, from which we can clearly see the uniform distribution of nickel, cobalt and oxygen of $NiCo_2O_4$ nanocages.

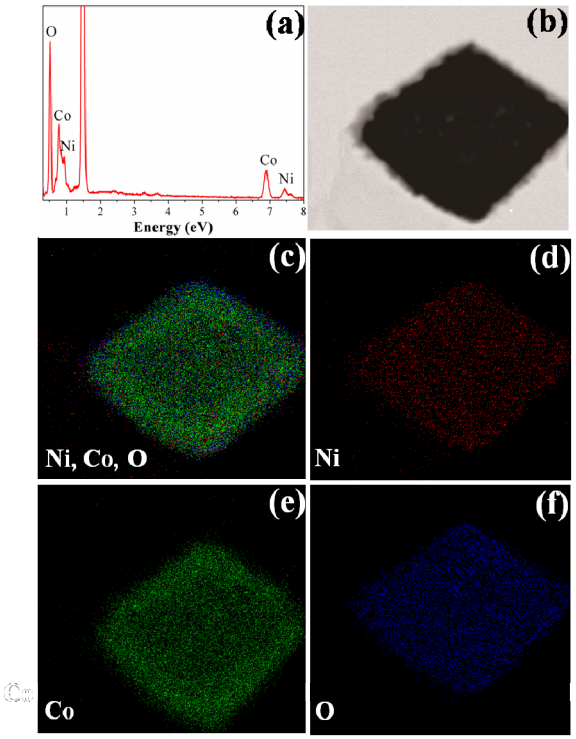

Figure 3. EDX spectrum, in which the Cu signal has originated from the copper grid (a), STEM images (b) and elemental maps (c-f) for mixed, Ni, Co, O respectively of the octahedral $NiCo_2O_4$ nanocages.

To obtain detailed information about the elemental character and oxidation state of the as-prepared $NiCo_2O_4$ samples, XPS measurements were performed and results are presented in Figure 4. The survey spectrum (Figure 4a) indicates the presence of Ni, Co and O as well as C from the reference and the absence of other impurities.[22, 27, 40] In the Ni 2p spectra (Figure 4b), two kinds of nickel species containing Ni^{2+} and Ni^{3+} can be observed. The fitting peeks at 854.0 eV and 871.7 eV are indexed to Ni^{2+}, while the fitting peaks at 855.9 eV and 873.8 eV are indexed to Ni^{3+}.[22, 40] The peaks at around 861.0 eV and 879.4 eV are two shake-up type peaks of nickel at the high binding energy side of the Ni $2p_{3/2}$ and Ni $2p_{1/2}$ edge. In the Co 2p spectra (Figure 4c), two kinds of Co species (Co^{2+} and Co^{3+}) were detected. The binding energies at 778.9 eV and 794.6 eV are ascribed to Co^{3+}. Another two fitting peaks at 781.2 eV and 797.3 eV are ascribed to Co^{2+}.[27, 40, 48] The high resolution spectrum for O1s (Figure 4d) shows three oxygen species marked as O1, O2 and O3. According to previous reports, the fitting peak of O1 at a binding energy at 529.6 eV is a typical metal-oxygen bond,[21, 27,40] O2 at a binding energy of 531.3 eV is usually associated with defects, contaminants, and a number of surface species including hydroxyls, chemisorbed oxygen, under-coordinated lattice oxygen, or species intrinsic to the surface of the spinel.[21, 27, 40] The peaks of O3 at ~532.8 eV can be attributed to multiplicity of physi- and chemi-sorbed water at or near the surface.[21, 27, 40] Moreover, the total atomic ratio of Ni and Co elements is ca. 1:2.1 (Table S1), which is corresponding to the result (1:2) indicated by energy-dispersive X-ray spectroscopy (EDX).

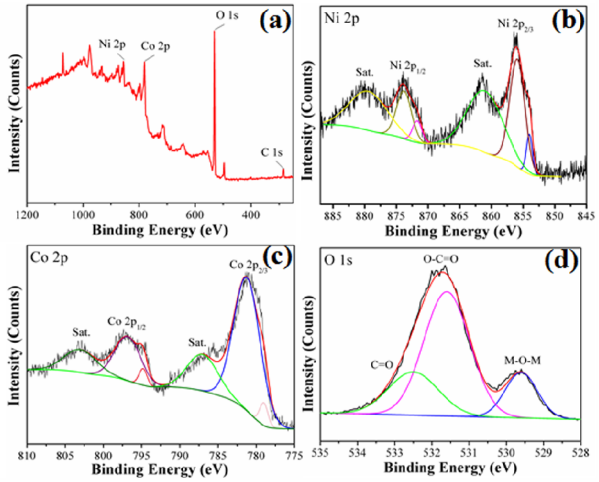

Figure 4. XPS spectrum of (a) survey spectrum, (b) Ni 2p, (c) Co 2p, and (d) O 1s for $NiCo_2O_4$ nanocages.

Here we also confirm the porosity of $NiCo_2O_4$ nanocages by N_2 adsorption-desorption isotherm curves. As shown in Figure 5, the N_2 adsorption-desorption isotherm is characteristic of type IV with a typical H_2 hysteresis loop observed in the range 0.8-1.0 p/p_0.[27, 40] This result suggests that the as-prepared $NiCo_2O_4$ nanocages have a typical mesoporous structure. The inset in the Figure 5 shows the corresponding pore size distribution calculated by the Barrett-Joyner-Halenda (BJH) method from the desorption branch, indicating a narrow pore size distribution (2-25 nm) centered at around 2 nm, which is good for the diffusion of active species in electrode materials.[14, 22, 49], It can be concluded that the sample is characteristic of mesoporous materials. According to the BET results, the $NiCo_2O_4$ microspheres give rise to a relatively high Brunauer-Emmett-Teller (BET) specific surface area (SSA) of 71.5 m^2g^{-1}. The mesoporous structure and large SSA not only greatly improve the electrode-electrolyte contact area, but also afford enough active sites for oxygen evolution reaction.[27] Therefore, the $NiCo_2O_4$ nanocage catalyst might have huge potential for the oxygen evolution reaction.

To study the electrocatalytic activity of $NiCo_2O_4$ nanocage for OER, liner sweep voltammetry (LSV) measurements were conducted on the glassy carbon electrodes in an O_2-saturated 0.1 M KOH within the potential range of 1.0 to 2.0 V (vs RHE). (see Experimental Section for details).[35,41] The ohmic potential drop (iR) loss that arises from the solution resistance were all corrected (Supporting Information, Figure S2). The overpotential at current density of 10 mA cm^{-2} and Tafel slope ($\log j$ -η) are usually used to estimate the oxygen evolution reaction activity.

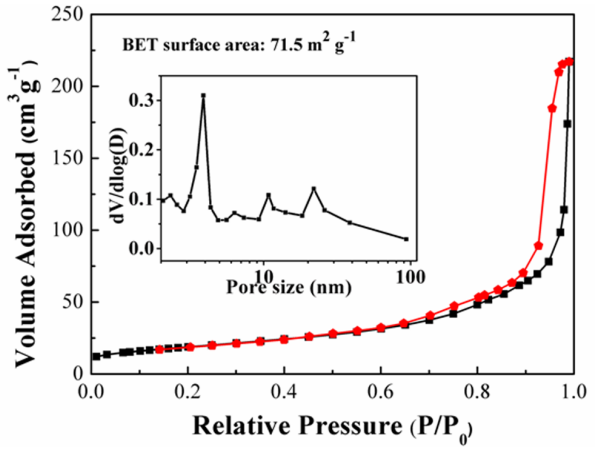

Figure 5. Nitrogen adsorption-desorption isotherm and the corresponding pore size distribution (inset) of $NiCo_2O_4$ mesoporous microspheres.

In order to elucidate the effect of the nanocage structure and the Ni incorporation, the $NiCo_2O_4$ nanoparticles and Co_3O_4 nanocages were prepared and their LSVs for OER were also tested for comparison (Figure 6a). The $NiCo_2O_4$ nanocages exhibit a lower overpotential of ~0.34 V at the current density of 10 mA cm^{-2} and a Tafel slope of 75 mV dec^{-1} compared to those of Co_3O_4 nanocages (~0.42 V and 110 mV dec^{-1}) (Figure 6b, Table 1). This enhancement in OER activity is due to the Ni species in the octahedral sites of the spinel, which creates active sites for OER with much lower activation potential compared to that of the Co cation.[27] In addition, the nanocage structure of $NiCo_2O_4$ is highly beneficial for the enhancement of OER activity since the $NiCo_2O_4$ nanoparticles (without PVP) (Figure S3) show a higher overpotential of ~0.422 V and bigger Tafel slope of 136 mV dec^{-1}(Figure 6a, 6c, Table 1). The enhanced OER performance of $NiCo_2O_4$ nanocage is ascribed to more efficient active sites with much lower energy barrier created by the characteristic $NiCo_2O_4$ nanocage. Moreover, the PVP polymer molecules can absorb on the surface of the $NiCo_2O_4$ nanograins and play the role of bridges connecting the adjacent nanograins together, thus keeping the nanocage shape of the $NiCo_2O_4$ shells.[42] Thus leading to confinement of the reactants within the inner space, resulting in the higher instantaneous concentration of reactants and products in the nanoreactors, providing a driving force to accelerate the catalytic reaction.[22] For comparison, similar measurements for 20 wt% Pt/C catalysts were also performed. As shown in Figure 6a, 6b, the commercial Pt/C, a classical catalyst for oxygen reduction reaction (ORR), bears only low OER activity. Thus, $NiCo_2O_4$ nanocages afford the largest oxygen-evolving current among all the studied catalysts.

To investigate the catalyst durability for OER, we performed accelerated stability tests in O_2-saturated 0.1 M KOH at room temperature for $NiCo_2O_4$ nanocages with other samples and Pt/C as references. As shown in Figure 6c, after 500 cycles, the $NiCo_2O_4$ nanocage became stable and exhibits only a mere several mV increase in η to achieve the current density of 10 mA cm^{-2}, so does the Co_3O_4 nanocage (Figure 6c-d). For $NiCo_2O_4$ nanoparticles (Figure 6c), the OER current decreases quickly during the following cycles, after 500 cycles, the $NiCo_2O_4$ nanoparticles exhibits a 20 mV increase in η to achieve the current density of 10 mA cm^{-2}. As to 20 wt% Pt/C, it also degrades quickly with continued LSV cycling and fails to reach the current density of 10 mA cm^{-2} after 500 cycles (Figure 6d).

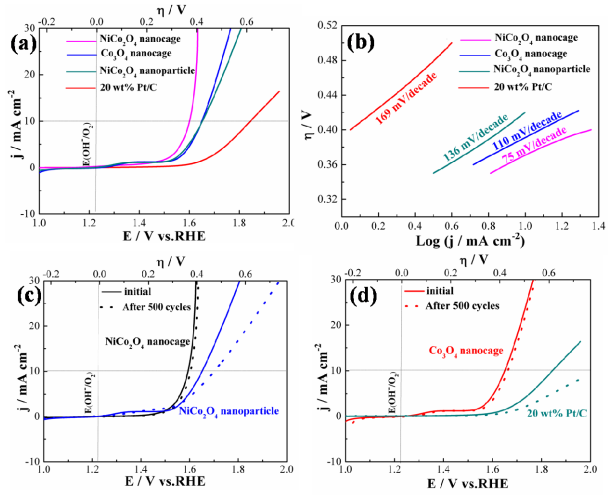

Figure 6. (a) Comparison of oxygen evolution currents for $NiCo_2O_4$ nanocage, Co_3O_4 nanocage, $NiCo_2O_4$ nanoparticles as well as 20 wt% Pt/C catalysts; (b) Tafel plots (η vs. Log current) of OER currents derived from (a); Oxygen evolution currents for (c) $NiCo_2O_4$ nanocage, $NiCo_2O_4$ nanoparticle and (d) Co_3O_4 nanocage and 20 wt% Pt/C before and after potential sweeps. All the measurements were performed in O_2-purged 0.1 M KOH (pH ~ 13). Oxygen evolution current curved were *i*R compensated.

These results suggest that the microstructure of the electrocatalyst has a significant influence on the stability of the electrode. Owing to the unique structure of nanocage, the three-dimensional hollow cages could effectively prevent aggregation of $NiCo_2O_4$ nanoparticles which are connected by PVP. Additionally, the thin and porous shell connect the cavities to form the three-dimensional interconnected pore structure, which is conducive to the efficient oxygen diffusion and consequently leads to superior stability of the electrode. Conversely, the $NiCo_2O_4$ nanoparticles tend to aggregate and thus many paths for oxygen diffusion are randomly created during oxygen generation and diffusion, which significantly damages the electrode.[23]

To better compare and understand the oxygen evolution reaction ability, the potential and overpotential (η) at a current density of 10 mA cm^{-2}, the Tafel slopes for OER of the above catalysts are all presented in Table 1. Remarkably, the $NiCo_2O_4$ nanocages exhibits a small overpotential of 340 mV and a Tafel slope of 75 mV dec^{-1}, such performance is even comparable to those of the best reported transition metal oxides based catalysts in previous literatures, though there is still significant room for improving the OER activity when comparing with the IrO_x catalysts. (Table S2), indicating the excellent OER catalytic activity of the $NiCo_2O_4$ nanocages.

Table 1. Comparison of OER Activity Data for Different Catalysts in this study[a].

Catalysts	η (mV) at J = 10 mA cm^{-2}	Tafel slope (mV dec^{-1})	E_{OER} (V) at J = 10 mA cm^{-2}
$NiCo_2O_4$ nanocage	340	75	1.568
Co_3O_4 nanocage	420	110	1.648
$NiCo_2O_4$ nanoparticles	422	136	1.650
20 wt% Pt/C	600	169	1.828

[a]All the potential values here were vs. RHE for comparison.

The excellent OER activity for that hollow $NiCo_2O_4$ nanocages

could be ascribed to their unique composition and structure. First, the incorporation of Ni cations into the octahedral sites of the spinel crystal structure increases the electrical conductivity and the creation of new active sites with much lower activation energy, and thus enhances the OER activity.[27] Second, the hollow structure offers sufficient void space, which leads to the confinement of the reactants to the inner space, resulting in the higher instantaneous concentration of reactants and products in the nanoreactors, providing a driving force to accelerate the oxygen evolution reaction.[23,42] Third, the decomposition of the surface absorbed PVP during the calcination process creates uniformly distributed meso-sized pores. The mesoporous structure with high surface area could provide higher surface density of catalytic active sites exposed to the OER-relevant species (O_2, OH-, e^-, H_2O) and promote the mass transport rate, which leads to enhanced catalytic activity.[35]

4. Conclusions

A novel and facile strategy for fabrication of hollow mesoporous $NiCo_2O_4$ nanocages as high-performance OER catalysts is reported. The $NiCo_2O_4$ nanocages exhibited outstanding OER electrochemical activity with a small overpotential of ~0.34 V at the current density of 10 mA cm^{-2}, which is more efficient than Co_3O_4 nanocage, $NiCo_2O_4$ nanoparticles, and the commercial 20 wt% Pt/C. This nanocatalyst is even comparable to those of the best reported transition metal oxides based catalysts in previous literatures. The superior electrocatalytic activity and stability of $NiCo_2O_4$ nanocages can be attributed to its unique hollow mesoporous structure and the efficient elemental composition. Our studies demonstrate the fabrication of a high-efficiency and low-cost non-precious metal OER catalyst that could be applicable in energy conversion technologies.

Acknowledgements

This work was supported by the National Natural Science Foundation of China (21471056, 21236003, 21206042, 20925621, and 21176083), the Basic Research Program of Shanghai (13NM1400700, 13NM1400701), and the Fundamental Research Funds for the Central Universities.

Notes and references

Key Laboratory for Ultrafine Materials of Ministry of Education, School of Materials Science and Engineering, East China University of Science and Technology, Shanghai 200237, China. E-mail: yhzhu@ecust.edu.cn; xlyang@ecust.edu.cn; Fax: +86 21 6425 0624; Tel: +86 21 6425 2022

† Electronic Supplementary Information (ESI) available: See DOI: 10.1039/b000000x/

1. M. G. Walter, E. L. Warren, J. R. Mckone, S. W. Boettcher, Q. Mi, E. A. Santori and N. S. Lewis, *Chem. Rev*., 2010, **110**, 6446.
2. T. R. Cook, D. K. Dogutan, S. Y. Reece, Y. Surendranath, T. S. Teets and D. G. Nocera, *Chem. Rev*., 2010, **110**, 6474.
3. H. Dau, C. Limberg, T. Reier, M. Risch, S. Roggan and P. Strasser, *ChemCatChem*, 2010, **2**, 724.
4. M. Gong, Y. Li, H. Wang, Y. Liang, J. Z. Wu, J. Zhou, J. Wang, T. Regier, F. Wei and H. Dai, *J. Am, Chem, Soc*., 2013, **135**, 8452.
5. J. Suntivich, K. J. May, H. A. Gasteiger, J. B. Goodenough and Y. Shao-Horn, *Science*, 2011, **334**, 1383.
6. E. Mirzakulova, R. Khatmullin, J. Walpita, T. Corrigan, N. M. Vargas-Barbosa, S. Vyas, S. Oottikkal, S. F. Manzer, C.M. Hadad and K. D. Glusac, *Nat. Chem*., 2012, **4**, 794.
7. S. W. Lee, C. Carlton, M. Risch, Y. Surendranath, S. Chen, S. Furutsuki, A. Yamada, D. G. Nocera and Y. Shao-Horn, *J. Am. Chem. Soc*., 2012, **134**, 16959.
8. Y. M. Lee, J. Suntivich, K. J. May, E. E. Perry and Y. Shao-Horn, *J. Phys. Chem. Lett*., 2012, **3**, 399.
9. W. H. Lee and H. Kim, *Catal. Commun*., 2011, **12**, 408.
10. W. Hu, Y. Q. Wang, X. H. Hu, Y. Q. Zhou and S. L. Chen, *J. Mater. Chem*., 2012, **22**, 6010.
11. Y. Tan, C. Xu, G. Chen, X. Fang, N. Zheng and Q. Xie, *Adv. Funct. Mater*., 2012,**22**, 4584.
12. C. Jin, F. Lu, X. Cao, Z. Yang and R. Yang, *J. Mater. Chem. A*, 2013, **1**, 12170.
13. G. -L. Tian, M. -Q. Zhao, D. Yu, .X. -Y. Kong, J. -Q. Huang, Q. Zhang and F. Wei, *Small*, 2014, **10**, 2251.
14. Y. Li, P. Hasin and Y. Wu, *Adv. Mater*., 2010, **22**, 1926.
15. B. S. Yeo and A. T. Bell, *J. Am. Chem. Soc*., 2011, **133**, 5587.
16. S. R. Mellsop, A. Gardiner and A. T. Marshall, *Electrocatalysis*, 2014, **5**, 445.
17. B. Cui, H. Lin, J. -B. Li, X. Li, J. Yang and J. Tao, *Adv. Funct. Mater*., 2008, **18**, 1440
18. F. Jiao and H. Frei, *Angew. Chem. Int. Ed*., 2009, **48**, 1841.
19. N. I. Andersen, A. Serov and P. Atanassov, *Appl. Catal., B: Environ.,* 2015, **163**, 623.
20. X. Wu and K. Scott, *J. Mater. Chem*., 2011, **21**, 12344.
21. M. Prabu, K. Ketpang and S. Shanmugam , *Nanoscale*, 2014, **6**, 3173.
22. L. Qian, L. Gu, L. Yang, H. Yuan and D. Xiao, *Nanoscale*, 2013, **5**, 7388.
23. J. Wang, T. Qiu, X. Chen, Y. Lu and W. Yang, *J. Power. Sources*, 2014, **268**, 341.
24. Y. Liang, Y. Li, H. Wang, J. Zhou, J. Wang, T. Regier and H. Dai, *Nat. Mater*., 2011, **10**, 780.
25. M. W. Kanan, D. G. Nocera, *Science*, 2008, **321**, 1072.
26. B. Sun, J. Q. Zhang, P. Munroe, H. J. Ahn and G. X. Wang, *Electrochem. Commun*., 2013, **31**, 88.
27. D. U. Lee, B. J. Kim and Z. W. Chen, *J. Mater. Chem. A*, 2013, **1**, 4754.
28. G. B. Sun, B. X. Dong, M. H. Cao, B. Q. Wei and C. W. Hu, *Chem. Mater*., 2011, **23**, 1587.
29. A. Q. Pan, H. B. Wu, L. Zhang and X. W. Lou, *Energ. Environ. Sci*., 2013, **6**, 1476.
30. J. Sun, H. M. Liu, X. Chen, D. G. Evans and W. S. Yang, *Nanoscale*, 2013, **5**, 7564.
31. X. W. Lou, L. A.. Archer and Z. Zhang, *Adv. Mater*., 2008, **20**, 3987.
32. S. E. Skrabalak, J. Chen, Y. Sun, X. Lu, L. Au, C. M. Cobley and Y. Xia, *Acc. Chem. Res*., 2008, **41**, 1587
33. O. Shchepelina, V. Kozlovskaya, S. Singamaneni, E. Kharlampieva and V. V. Tsukruk, *J. Mater. Chem*., 2010, **20**, 6587.
34. Z. Wang and X. W. Lou, *Adv. Mater*., 2012, **24**, 4124.
35. Y. Su, Y. Zhu, H. Jiang, J. Shen, X. Yang, W. Zou, J. Chen and C. Li, *Nanoscale*, 2014, **6**, 15080.
36. J. Nai, Y. Tian, X. Guan and L. Guo, *J. Am. Chem. Soc*., 2013, **135**, 16082.
37. B. Liu, H. C. Zeng, *J. Am. Chem. Soc*., 2004, **126**, 8124.
38. X. Yu, X. Yao, T. Luo, Y. Jia, J. Liu and X. Huang, *ACS Appl. Mater. Inter.*, 2014, **6**, 3689.
39. H. Guo, L. Liu, T. Li, W. Chen, J. Liu, Y. Guo and Y. Guo, *Nanoscale*, 2014, **6**, 5491.
40. J. Li, S. Xiong, Y. Liu, Z. Ju and Y. Qian, *ACS Appl. Mater. Inter.*, 2013, **5**, 981.
41. M. Gao, W. Sheng, Z. Zhuang, Q. Fang, S. Gu, J. Jiang and Y. Yan, *J. Am, Chem. Soc*., 2014, **136**, 7077.
42. X. Lv, Y. Zhu, H. Jiang, H. Zhong, X. Yang and C. Li, *Dalton Trans*., 2014, **43**, 15111
43. T. Maiyalagan, K. R. Chemelewski and A. Manthiram, *ACS Catal*., 2014, **4**, 421.
44. S. Chen and S. Qiao, *ASC Nano*, 2013, **7**, 10190.
45. M. Gao, Y. Xu, J. Jiang, Y. Zheng and S. Yu, *J. Am. Chem. Soc*., 2012, **134**, 2930.
46. X. Liu, Z. Chang, L. Luo, T. Xu, X. Lei, J. Liu and X. Sun, *Chem. Mater*., 2014, **26**, 1889.

47. Z. Zhang, X. Wang, G. Cui, A. Zhang, X. Zhou, H. Xu and L. Gu, *Nanoscale*, 2014, **6**, 3540.
48. W. Wei, L. Mi, Y. Gao, Z. Zheng, W. Chen and X. Guan, *Chem. Mater*., 2014, **26**, 3418.
49. H. Jiang, J. Ma and C. Z. Li, *Chem. Commun*., 2012, **48**, 4465.